J Med Syst (2017) 41: 168
DOI 10.1007/s10916-017-0816-2

EDUCATION & TRAINING

Mathematical Development and Computational Analysis of Harmonic Phase-Magnetic Resonance Imaging (HARP-MRI) Based on Bloch Nuclear Magnetic Resonance (NMR) Diffusion Model for Myocardial Motion

Michael O. Dada[1] **· Babatunde Jayeoba**[1] **· Bamidele O. Awojoyogbe**[1,2] **·**
Uno E. Uno[1] **· Oluseyi E. Awe**[3]

Received: 20 September 2015 / Accepted: 1 September 2017 / Published online: 13 September 2017

Abstract Harmonic Phase-Magnetic Resonance Imaging (HARP-MRI) is a tagged image analysis method that can measure myocardial motion and strain in near real-time and is considered a potential candidate to make magnetic resonance tagging clinically viable. However, analytical expressions of radially tagged transverse magnetization in polar coordinates (which is required to appropriately describe the shape of the heart) have not been explored because the physics required to directly connect myocardial deformation of tagged Nuclear Magnetic Resonance (NMR) transverse magnetization in polar geometry and the appropriate harmonic phase parameters are not yet available. The analytical solution of Bloch NMR diffusion equation in spherical geometry with appropriate spherical wave tagging function is important for proper analysis and monitoring of heart systolic and diastolic deformation with relevant boundary conditions. In this study, we applied Harmonic Phase MRI method to compute the difference between tagged and untagged NMR transverse magnetization based on the Bloch NMR diffusion equation and obtained radial wave tagging function for analysis of myocardial motion. The analytical solution of the Bloch NMR equations and the computational simulation of myocardial motion as developed in this study are intended to significantly improve healthcare for accurate diagnosis, prognosis and treatment of cardiovascular related deceases at the lowest cost because MRI scan is still one of the most expensive anywhere. The analysis is fundamental and significant because all Magnetic Resonance Imaging techniques are based on the Bloch NMR flow equations.

Keywords Bloch NMR diffusion equation · Myocardial motion · HARP-MRI · Magnetic resonance tagging · Mathematica

Introduction

The description and understanding of cardiac anatomy and function are challenging tasks due to the complexity of the heart and the cardiovascular system. Accurate knowledge of the heart functionality is of great importance for improving medical diagnosis and treatment of cardiovascular diseases. Alterations in the myocardial motion pattern are often early and sensitive indicators for cardiac disease such as reduced myocardial perfusion due to coronary artery stenosis or acute allograft rejection after heart transplantation [1].

Moreover, assessment of left ventricular dyssynchrony can be an important factor for determining long term prognosis and optimal treatment after myocardial infarction and can give valuable insights with regard to cardiac re-synchronization.

Many cardiac diseases can affect the systolic function of the heart. A patient may have significant regional dysfunction while maintaining an ejection fraction within normal limits. Assessment and quantification of cardiac function is thus important for diagnosis and treatment of heart disease.

This article is part of the Topical Collection on *Education & Training*

✉ Bamidele O. Awojoyogbe
abamidele@futminna.edu.ng; awojoyogbe@yahoo.com

[1] Department of Physics, Federal University of Technology, Minna, Niger State, Nigeria

[2] Department of Physics, University of Ilorin, Ilorin, Kwara State, Nigeria

[3] Department of Physics, University of Ibadan, Ibadan, Oyo State, Nigeria

The three-dimensional motion of the curved heart wall through the fixed imaging plane can affect the apparent local motion in the two-dimensional image. In addition, the lack of identifiable landmarks within the heart wall makes assessment of motion very limited, once we have imaged the heart during the cardiac cycle we want to calculate the relative deformation of the myocardium between two different time frames. The primary problem is that the myocardium is uniform, providing few readily identifiable features in the images, and this brings about the use of non-invasive method of identification called tagging.

Magnetic resonance signals are results of the dynamics of atomic and the surrounding magnetic field it experiences [2]. Hence, other determinants of magnetic response of atoms include blood flow, chemistry, chemical exchange, diffusion and other physiological phenomena. These molecular signatures are very important for molecular imaging. An image containing information about these molecular parameters would definitely prove to be very important in detail understanding of how tissues and organs function, both normally and in disease conditions. Molecular MRI has been at the centre of different MRI techniques which have been developed and rapidly advancing with the aim of elucidating changes in these phenomena with emphasis on different physiological states or differential diagnosis of disease [2].

Magnetic resonance tagging (MR) tagging has evolved as a gold standard in diagnosis and characterization of CAD [3]. However, in comparison to echocardiography, the use of tagging has been very limited in the clinical setting. One of the outstanding issues has been long imaging times and even longer post-processing times. Long imaging times are often accompanied with patient discomfort and can yield motion corrupted images. The discovery of Harmonic phase (HARP) MRI has changed this situation. HARP-MRI is a tagged image analysis method that can measure myocardial motion and strain in near real-time and is seen as a potential candidate to make MR tagging clinically viable [1].

Tagged MRI is a non-invasive technique that has the potential to significantly improve the evaluation of cardiac function, including the ability to provide novel information about regional function. Indeed, MR Tagging can be used to track specific myocardial points throughout the cardiac cycles without the use of invasive landmarks such as radiopaque markers or sonomicrometers.

With the introduction of Harmonic Phase (HARP) processing [1], fast and reliable tracking of arbitrary landmark points has become possible and user interaction could be drastically reduced compared to other techniques.

During the cardiac cycle, the heart performs a complex three-dimensional motion pattern caused by the particular arrangement of myocardial fibres. The overall uniform circumferential contraction of the healthy left ventricle with more endo- and less epicardial deformation is accompanied by longitudinal shortening and a wringing motion between base and apex during systole. In the diseased state, this contraction pattern often presents with significantly altered properties [4]. In order to assess the motion of the entire left ventricle and to capture possible regional motion defects, multiple tagged slices need to be acquired in different orientations. This combination of two-dimensional techniques often leads to slice mis-registration problems and long acquisition times. Alternatively, tagging preparation can be applied in three dimensions and a volume of the whole heart can directly be acquired. This technique successfully addresses slice registration issues but overall scan times are too long for application in patients and in larger clinical studies, this brings about HARP as a remedy. With the introduction of Harmonic Phase (HARP) processing, fast and reliable tracking of arbitrary landmark points has become possible and user interaction could be reduced significantly compared to other techniques [1].

Further development of tagging acquisition and post-processing methods along with their applications in clinical studies is of great interest in clinical cardiology. The requirement to fit the entire tagging examination within a few short breath-holds is of particular importance as many of the patients are unable to sustain breath-holds over extended periods.

The NMR transverse magnetization carries lots of information on the properties, structures of materials and material medium. This has been demonstrated by many experiments on porous media [5–7], but analytical expressions of radially tagged transverse magnetization in polar coordinates has not been explored to show the direct relationship between myocardial deformation of tagged magnetization in polar geometry and the Harmonic Phase parameters. The analytical solution of NMR Bloch diffusion equation in spherical geometry and analysis of appropriate spherical wave tagging function is important for the accurate analysis/monitoring of heart systolic and diastolic deformation with related conditions.

In this study, based on the analytical solution of the fundamental Bloch NMR flow equation, new approach to analyze cardiac tagged MRI using the concept of harmonic phase (HARP) images would be developed with radial/spherical wave tagging function for myocardial motion. The Harmonic Phase MRI tagging function will be used to compute (i) the difference between tagged and untagged magnetization, (ii) magnetic resonance harmonic phase velocity and (iii) myocardial radial strain functions. These will be useful for the design and evaluation of new therapies for impaired cardiac function.

Bloch NMR diffusion model

All MRI concepts, dynamics and experiments are governed by the Bloch NMR equations. These equations relate the macroscopic model of magnetization to the applied radiofrequency, gradient and static magnetic fields. The dynamics of the changes in bodies containing NMR - sensitive nuclei, its physical changes (for example, freely diffusing or bound within a cavity) are carefully captured by the Bloch NMR equation: a phenomenological equation describing the physics of magnetic moments – such as the moment of water proton as a precessional gyroscopic motion in the presence of exponential damping (T_1 and T_2), perturbing magnetic fields (the fixed B_o, and the time -varying radiofrequency B_1).

The Bloch NMR diffusion model is obtained from a general second order differential equation derived from NMR Bloch equations that can be applied to myocardial motion under the appropriate boundary conditions [8–14].

Magnetic Resonance (MR) tagged image can be explained as a combination of anatomy component and the tagging component that is overlaid on the anatomy. The anatomy component is derivable from the Bloch NMR diffusion model obtained from the Bloch NMR flow equation:

$$v^2\frac{\partial M_y}{\partial x^2}+2v\frac{\partial^2 M_y}{\partial x\partial t}+v\left(\frac{1}{T_1}+\frac{1}{T_2}\right)\frac{\partial M_y}{\partial x}+\left(\frac{1}{T_1}+\frac{1}{T_2}\right)\frac{\partial M_y}{\partial t}+\frac{\partial^2 M_y}{\partial t^2}+\left(\frac{1}{T_1T_2}+\gamma^2{B_1}^2\right)M_y=\frac{\gamma B_1 M_o}{T_1} \tag{1a}$$

Equation (1a) can be written as:

$$v^2\frac{\partial^2 M_y}{\partial x^2}+2v\frac{\partial^2 M_y}{\partial x\partial t}+vT_0\frac{\partial M_y}{\partial x}+T_0\frac{\partial M_y}{\partial t}+\frac{\partial^2 M_y}{\partial t^2}+\left(T_g+\gamma^2{B_1}^2\right)M_y=F_0\gamma B_1 \tag{1b}$$

where $T_0=\frac{1}{T_1}+\frac{1}{T_1}$, $T_g=\frac{1}{T_1T_2}$ and $F_0=\frac{M_0}{T_1}$.

Equation (1b) is a general second order partial differential equation (Awojoyogbe-Bloch NMR flow equation) derived from NMR Bloch equation that can be applied to any fluid flow problem [8–11]. γ is the gyromagnetic Ratio, v is the fluid velocity, T_1 and T_2 are spin lattice and spin spin relaxation times respectively, M_y is the Nuclear magnetic Resonance (NMR) transverse magnetization. At any given time t, we can obtain information about the system, if appropriate boundary conditions are applied [12–14]. The term $F_0\gamma B_1(x,t)$ is the forcing function. If this function is zero, a freely vibrating system results; else, the system is undergoing a forced vibration.

Equation (1b) is applicable under the following conditions:

(i) The selected slice must be homogeneous with one compartment (either of tissue or of fluid compartment).
(ii) Rate of fluid influx and efflux should be very small and equal (such as in some slow blood flow junctions) or static fluid (e.g. edema).
(iii) The size of the chemical substance to be investigated must be significantly very small compared to the tissue compartment in which they are found.
(iv) The geometry of the compartment should be defined and could be approximated to common geometrical system.

Assuming that the excitation coil is large enough to cover the slice under investigation, the amount of radiofrequency (RF) power received by any of the fluid particles should be the same irrespective of the position of the particle spin. The NMR diffusion model was derived from Eq. (1b) as follows [11–14]:

$$\frac{\partial M_y}{\partial t}=D\nabla^2 M_y+\frac{F_0}{T_0}\gamma B_1\left(\vec{r},t\right) \tag{2a}$$

provided that

$$D=\frac{-v^2}{T_0} \tag{2b}$$

where $F_0=\frac{M_0}{T_1}$, $T_0=\frac{1}{T_1}+\frac{1}{T_1}$, M_0 is equilibrium magnetization, T_1 is spin-lattice relaxation time while T_2 is spin-spin relaxation time.

In Eq. (2b), D represents the diffusion coefficient and Eq. (2a) becomes the diffusion equation for magnetization as the nuclear spins are in motion. ∇^2 is the Laplacian operator in the specified coordinate, t is the diffusion time while x is the diffusion distance [11–13]. The coordinate of this equation in common geometries are given as follows:

Cartesian Geometry : (3)

$$\frac{\partial M_y}{\partial t}=D\left(\frac{\partial^2 M_y}{\partial x^2}+\frac{\partial^2 M_y}{\partial y^2}+\frac{\partial^2 M_y}{\partial z^2}\right)+\frac{F_o}{T_o}\gamma B_1\left(\vec{r},t\right)$$

Cylindrical Geometry : (4)

$$\frac{\partial M_y}{\partial t}=D\left(\frac{1}{r}\frac{\partial}{\partial r}\left(r\frac{\partial M_y}{\partial r}\right)+\frac{1}{r^2}\frac{\partial^2 M_y}{\partial \phi^2}+\frac{\partial^2 M_y}{\partial z^2}\right)+\frac{F_o}{T_o}\gamma B_1(x,t)$$

$$\textit{Spherical Geometry}: \tag{5}$$

$$\frac{\partial M_y}{\partial t} = \frac{D}{r^2}\left(\frac{\partial}{\partial r}\left(r^2\frac{\partial M_y}{\partial r}\right) + \frac{1}{\sin^2\theta}\frac{\partial^2 M_y}{\partial \phi^2} + \frac{1}{\sin\theta}\frac{\partial}{\partial \theta}\left(\sin\theta\frac{\partial M_y}{\partial \theta}\right)\right) + \frac{F_o}{T_o}\gamma B_1\left(\overrightarrow{r}, t\right)$$

Anatomy component of MRI in spherical geometry

The NMR diffusion equation within a spherical cavity is solved for the anatomy component of MR tagged image as in the case of myocardial geometry given in Eq. (2). Since Eq. (2) is a linear second order differential equation, it can be written as a linear summation given by [14, 15]:

$$M_y = M_{yy}\left(\overrightarrow{r}, t\right) + \Omega\left(\overrightarrow{r}\right) \tag{6}$$

$$\frac{\partial M_y}{\partial t} = \frac{\partial M_{yy}}{\partial t} \tag{7}$$

$$\nabla^2 M_y = \nabla^2 M_{yy} + \frac{d^2\Omega}{dr^2} \tag{8}$$

If the RF field varies with spatial coordinates and remains constant with time, we write

$$\frac{\partial M_y}{\partial t} = D\nabla^2 M_y + \gamma B_1\left(\overrightarrow{r}\right) \tag{9}$$

From Eqs. (7), (8) and (9), we obtain:

$$\frac{\partial M_{yy}}{\partial t} = D\left(\nabla^2 M_{yy} + \frac{d^2\Omega}{dr^2}\right) + \frac{F_0}{T_0}\gamma B_1\left(\overrightarrow{r}\right) \tag{10}$$

$$\frac{\partial M_{yy}}{\partial t} = D\nabla^2 M_{yy} \tag{11a}$$

where

$$D\frac{d^2\Omega}{dr^2} = -\frac{F_0}{T_0}\gamma B_1\left(\overrightarrow{r}\right) \tag{11b}$$

Performing the integration in Eq. (11b) gives

$$d\Omega = -\frac{F_0}{T_0}\int\frac{\gamma B_1\left(\overrightarrow{r}\right)}{D}rdr$$

If the RF gradient is applied in radial direction, the pulse becomes r-dependent as follows [16]:

$$B_1\left(\overrightarrow{r}\right) = B_1(r) = g_r r$$

where g_r represents the RF gradient magnitude.

$$\Omega = -\frac{F_0}{T_0}\left(\frac{\gamma g_r r}{D}\left(\frac{r^2}{2}\right)\right)$$

$$\Omega(r) = -\frac{F_0\gamma g_r r^3}{2DT_0} \tag{12}$$

$$D\nabla^2 M_{yy} = \frac{\partial M_{yy}}{\partial t}$$

Expanding Eq. (11a) in spherical coordinates leads to:

$$D\left(\frac{1}{r^2}\frac{\partial}{\partial r}\left(r^2\frac{\partial M_{yy}}{\partial r}\right) + \frac{1}{r^2\sin^2\theta}\frac{\partial^2 M_{yy}}{\partial \phi^2} + \frac{1}{r^2\sin\theta}\frac{\partial}{\partial \theta}\left(\sin\theta\frac{\partial M_{yy}}{\partial \theta}\right)\right) = \frac{\partial M_{yy}}{\partial t} \tag{13}$$

Equation (13) can be solved using separation of variable by assuming

$$M_{yy}(r, \theta, \phi, t) = G(r)\Theta(\theta)\Phi(\phi)T(t) \tag{14}$$

Making use of Eq. (14) in Eq. (13) gives:

$$\frac{1}{G}\frac{d^2G}{dr^2} + \frac{2}{rG}\frac{dG}{dr} + \frac{1}{r^2\sin^2\Theta}\frac{1}{\Phi}\frac{d^2\Phi}{d\phi^2} + \frac{1}{r^2\Theta}\frac{d^2\Theta}{d\theta^2} + \frac{\cot\Theta}{r^2\Theta}\frac{d\Theta}{d\theta} = \frac{1}{DT}\frac{dT}{dt} \tag{15}$$

Let Eq. (15) be equal to a dimensionless constant $-\lambda^2$ [17]

$$\frac{1}{T}dT = -\lambda^2 Ddt$$

The solution of which is given as:

$$T(t) = ae^{-\lambda^2 Dt} \tag{16}$$

Equating the left hand side of Eq. (15) to the same constant,$-\lambda^2$, we have

$$\frac{1}{G}\frac{d^2G}{dr^2} + \frac{2}{rG}\frac{dG}{dr} + \frac{1}{r^2\sin^2\Theta}\frac{1}{\Phi}\frac{d^2\Phi}{d\phi^2} + \frac{1}{r^2\Theta}\frac{d^2\Theta}{d\theta^2} + \frac{\cot\Theta}{r^2\Theta}\frac{d\Theta}{d\theta} + \lambda^2 = 0$$

Rearranging Eq. (16) gives

$$-\frac{1}{\sin^2\Theta}\frac{1}{\Phi}\frac{d^2\Phi}{d\phi^2} - \frac{1}{\Theta}\frac{d^2\Theta}{d\theta^2} - \frac{\cot\Theta}{\Theta}\frac{d\Theta}{d\theta} = \frac{r^2}{G}\frac{d^2G}{dr^2} + \frac{2r}{G}\frac{dG}{dr} + \lambda^2 r^2 \tag{17}$$

If Eq. (17) is equal to a constant $n(n+1)$,

$$r^2\frac{d^2G}{dr^2}+2r\frac{dG}{dr}+\left(\lambda^2r^2-n(n+1)\right)G=0 \tag{18}$$

Eq. (18) is the Spherical Bessel equation and can be transformed into Bessel differential equation as follows:

$$\Phi_r=\lambda r;\quad r\frac{dG}{dr}=\Phi_r\frac{dG}{d\phi_r}\text{ and }r^2\frac{d^2G}{dr^2}=\Phi_r\frac{d^2G}{dr^2} \tag{19}$$

where Φ is the phase function. Putting Eq. (19) into Eq. (18) [17], we obtain:

$$\Phi_r\frac{d^2G}{d\phi_r{}^2}+2\Phi_r\frac{dG}{dr}+\left(\Phi_r^2-n(n+1)\right)G=0$$

To solve this differential equation, we seek a solution of the form

$$G(r)=Y(\Phi_r)\Phi_r{}^{-\frac{1}{2}}$$

where

$$\frac{dG(r)}{d\Phi_r}=\frac{dY(\Phi_r)}{d\Phi_r}\Phi_r{}^{-\frac{1}{2}}-\frac{1}{2}Y(\Phi_r)\Phi_r{}^{-\frac{3}{2}} \tag{20}$$

$$\frac{d^2G(r)}{d\Phi_r^2}=\frac{d^2Y(\Phi_r)}{d\Phi_r^2}\Phi_r{}^{-\frac{1}{2}}-\frac{dY(\Phi_r)}{d\Phi_r}\Phi_r{}^{-\frac{3}{2}}+\frac{3}{4}Y(\Phi_r)\Phi_r{}^{-\frac{5}{2}} \tag{21}$$

Introducing Eqs. (20) and (21) into Eq. (18) leads to

$$\begin{aligned}&\Phi_r^2\left(\frac{d^2Y(\Phi_r)}{d\Phi_r^2}\Phi_r{}^{-\frac{1}{2}}-\frac{dY(\Phi_r)}{d\Phi_r}\Phi_r{}^{-\frac{3}{2}}+\frac{3}{4}Y(\Phi_r)\Phi_r{}^{-\frac{5}{2}}\right)+\\&2\Phi_r\left(\frac{dY(\Phi_r)}{d\Phi_r}\Phi_r{}^{-\frac{1}{2}}-\frac{1}{2}Y(\Phi_r)\Phi_r{}^{-\frac{3}{2}}\right)+\left(\Phi_r^2-n(n+1)\right)Y(\Phi_r)\Phi_r{}^{-\frac{1}{2}}=0\end{aligned} \tag{22a}$$

Multiply Eq. (22a) by $\Phi_r{}^{-\frac{1}{2}}$ gives

$$\begin{aligned}&\Phi_r^2\left(\frac{d^2Y(\Phi_r)}{d\Phi_r^2}-\frac{dY(\Phi_r)}{d\Phi_r}\Phi_r{}^{-1}+\frac{3}{4}Y(\Phi_r)\Phi_r{}^{-2}\right)\\&\quad+2\Phi_r\left(\frac{dY(\Phi_r)}{d\Phi_r}-\frac{1}{2}Y(\Phi_r)\Phi_r{}^{-1}\right)+\left(\Phi_r^2-n(n+1)\right)Y(\Phi_r)=0\end{aligned} \tag{22b}$$

Summing up similar terms in Eq. (22b) yields

$$\Phi_r^2\frac{d^2Y(\Phi_r)}{d\Phi_r^2}+\Phi_r\frac{dY(\Phi_r)}{d\Phi_r}+\left(\Phi_r^2-\left(n+\frac{1}{2}\right)^2\right)Y(\Phi_r)=0 \tag{22c}$$

Eq. (22c) is an ordinary Bessel differential equation of half-integral order [18]. The solutions to Eq. (22c) are the ordinary Bessel functions of half-integral order: $J_{n+\frac{1}{2}}$ and $N_{n+\frac{1}{2}}$. The solution to Eq. (22c) is:

$$Y(\Phi_r)=A_nJ_{n+\frac{1}{2}}(\Phi_r)+B_nN_{n+\frac{1}{2}}(\Phi_r) \tag{22d}$$

$J_{n+\frac{1}{2}}(\Phi_r)$ and $N_{n+\frac{1}{2}}(\Phi_r)$ are related to the spherical Bessel and Neuman functions (i.e. original solution of Eq. (18)) $j_n(\Phi_r)$ and $n_n(\Phi_r)$ where

$$j_n(\Phi_r)=\sqrt{\frac{\pi}{2}}\frac{J_{n+\frac{1}{2}}(\Phi_r)}{\sqrt{\Phi_r}} \tag{23}$$

$$n_n(\Phi_r)=\sqrt{\frac{\pi}{2}}\frac{N_{n+\frac{1}{2}}(\Phi_r)}{\sqrt{\Phi_r}} \tag{24a}$$

Putting Eqs. (23) and (24) into Eq. (22d), we obtain

$$Y(\Phi_r)=A_n\sqrt{\frac{2}{\pi}}\sqrt{\Phi_r}j_n(\Phi_r)+B_n\sqrt{\frac{2}{\pi}}\sqrt{\Phi_r}n_n(\Phi_r)$$

The Bessel functions $j_n(\Phi_r)$ are finite at the origin, but the Neuman's function has infinite values at the origin. Therefore, in order to always maintain a measurable NMR signal, we must set $B_n = 0$ and hence, the normalized solutions of Eq. (18) are:

$$G(r)=Y(\Phi_r)\Phi_r^{-\frac{1}{2}}=A_n\sqrt{\frac{2}{\pi}}j_n(\Phi_r) \tag{24b}$$

From Eq. (17), we may write:

$$-\frac{1}{\sin^2\Theta}\frac{1}{\Phi}\frac{d^2\Phi}{d\phi^2}-\frac{1}{\Theta}\frac{d^2\Theta}{d\theta^2}-\frac{\cot\Theta}{\Theta}\frac{d\Theta}{d\theta}=n(n+1) \tag{25}$$

$$\frac{\sin^2\Theta}{\Theta}\frac{d^2\Theta}{d\theta^2}+\sin^2\Theta\frac{\cot\Theta}{\Theta}\frac{d\Theta}{d\theta}+n(n+1)=-\frac{1}{\Phi}\frac{d^2\Phi}{d\phi^2} \tag{26}$$

Eq. (26) must be equal to a constant $-m^2$ and hence,

$$\frac{d^2\Phi}{d\phi^2}=-m^2\Phi$$

The solution of which is:

$$\Phi(\phi)=B_1\cos m\phi+B_2\sin m\phi \tag{27}$$

From Eq. (26), we write:

$$\frac{d^2\Theta}{d\theta^2}+\cot\Theta\frac{d\Theta}{d\theta}+n(n+1)\Theta-\frac{m^2}{\sin^2\Theta}\Theta=0$$

$$\frac{1}{\sin\theta}\frac{d}{d\theta}\left(\sin\theta\frac{d\Theta}{d\theta}\right)+\left(n(n+1)-\frac{m^2}{\sin^2\theta}\right)\Theta=0 \tag{28}$$

Setting $\varepsilon = \cos\theta$ [15, 16],

$$\frac{d\Theta}{d\theta}=\frac{d\Theta}{d\varepsilon}\frac{dz}{d\theta}=-\sin\theta\frac{d\Theta}{d\varepsilon};\quad \frac{d\varepsilon}{d\theta}=-\sin\theta\ ;\frac{d}{d\varepsilon}=-\frac{d}{\sin\theta d\theta}$$

$$\sin^2\theta=1-\varepsilon^2$$

The polar component in Eq. (14) becomes:

$$\frac{d}{d\varepsilon}\left(\left(1-\varepsilon^2\right)\frac{d\Theta}{d\varepsilon}\right)+\left(n(n+1)-\frac{m^2}{1-\varepsilon^2}\right)\Theta=0$$

$$\left(1-\varepsilon^2\right)\frac{d^2\Theta}{d\varepsilon^2}-2\varepsilon\frac{d\Theta}{d\varepsilon}+\left(n(n+1)-\frac{m^2}{1-\varepsilon^2}\right)\Theta=0 \tag{29}$$

Eq. (29) is known as Associated Legendre equation and the solution is given as:

$$\Theta(\theta)=C_1P_n^m(\cos\theta)+C_2Q_n^m(\cos\theta) \tag{30a}$$

where P_n^m and Q_n^m are associated Legendre functions of first and second kind respectively. Since it is required that the solution be finite on the polar axis of the myocardium, we write that $C_2 = 0$. Therefore, Eq. (30a) becomes

$$\Theta(\theta)=C_1P_n^m(\cos\theta) \tag{30b}$$

The general solution to Eq. (11a) is then the product of Eqs. (16), (24), (27) and (30b):

$$M_{yy}(r,\theta,\phi,t)=\left(A_n\sqrt{\frac{2}{\pi}}j_n(\Phi_r)\right)\left(C_1P_n^m(\cos\theta)\right) \tag{31}$$
$$\left(B_1\cos m\phi+B_2\sin m\phi\right)\left(ae^{-\lambda^2Dt}\right)$$

Finally, the general solution to Eq. (6) is given as:

$$M_y(r,\theta,\phi,t)=\left(A_n\sqrt{\frac{2}{\pi}}j_n(\Phi_r)\right)\left(C_1P_n^m(\cos\theta)\right) \tag{32}$$
$$\left(B_1\cos m\phi+B_2\sin m\phi\right)\left(ae^{-\lambda^2Dt}\right)-\frac{F_0\gamma g_r r^3}{2DT_0}$$

Boundary conditions for myocardial motion

Eq. (32) is a general analytical solution to the Bloch NMR diffusion equation. If the NMR transverse magnetization due to the tagging pulse applied at the point (R, θ, 2π) is nearly constant before the application of the imaging gradient pulse, we can write:

$$M_y(R,\theta,2\pi,0)=-\frac{F_0\gamma g_r}{2DT_0}R^3 \tag{33}$$

In Eq. (33a), the radius R indicates a point along the myocardial radial axis (the average radius of the endocardial compartment). Eq. (33) implies

$$M_{yy}(R,\theta,2\pi,0)=0\ \ or\ G(R)\Theta(\theta)\Phi(2\pi)T(0)=0 \tag{34}$$

It would be observed in Eq. (34) that in order to obtain an expression for M_{yy},

$$T(0)\neq 0\ \ \text{and}\ \Theta(\theta)\neq 0 \tag{35}$$

$$G(R)\ \ or\ \Phi(2\pi)=0 \tag{36}$$

For the condition $\Phi(2\pi) = 0$,

$$\Phi(\phi)=B_2\sin m\phi \tag{37}$$

Meanwhile, for the condition $G(R) = 0$,

$$A_nJ_{n+\frac{1}{2}}(\lambda R)=0 \tag{38}$$

Since $A_n \neq 0$, we write:

$$J_{n+\frac{1}{2}}(\varphi)=0 \tag{39}$$

where $\varphi = \lambda R$. The roots of the Bessel function are given as:

$$\varphi=\varphi_{nm};m=0,1,2,3,\ldots\ldots \tag{40}$$

Setting

$$\lambda=\frac{\phi_{nm}}{R} \tag{41}$$

If we now perform superposition of the solutions by summing over n and m [11], we have

$$M_{yy}(r,\theta,\phi,t)=\sum_{n=0}^{\infty}\sum_{m=0}^{\infty}A_{nm}J_{n+\frac{1}{2}}\left(\frac{\varphi_{nm}}{R}r\right) \tag{42}$$
$$\left[P_n^m(\cos\theta)\right]\left[\sin m\phi\right]e^{-\frac{\varphi_{nm}^2}{R^2}Dt}$$

Table 1 Estimated (radial) values of ventricular dilatation at diastole and systole [22]

	Female	Male
Left ventricle		
Diastolic	0.026 m	0.0304 m
Systolic	0.01875 m	0.0201 m
Right ventricle		
Diastolic	0.01915 m	0.02445 m
Systolic	0.01495 m	0.01845 m

where $A_{nm} = A_n C_1 B_2 a$. If we assume that at other points apart from $\phi = 2\pi$, we have the conditions

$$M_y\left(r, \theta, \frac{\pi}{2m}, 0\right) = M_p(r, \theta) - \frac{F_0 \gamma g_r}{2DT_0} r^3 \tag{43}$$

$$M_{yy}\left(r, \theta, \frac{\pi}{2m}, 0\right) = M_p(r, \theta) \tag{44}$$

Eq. (31) gives:

$$\begin{aligned} M_p(r,\theta) &= \sum_{n=0}^{\infty}\sum_{m=0}^{\infty} A_{nm} J_{n+\frac{1}{2}}\left(\frac{\varphi_{nm} r}{R}\right)\left[P_n^m(\cos\theta)\right]\sin\frac{\pi}{2} \\ &= \sum_{n=0}^{\infty}\sum_{m=0}^{\infty} A_{nm} J_{n+\frac{1}{2}}\left(\frac{\varphi_{nm} r}{R}\right)\left[P_n^m(\cos\theta)\right] \end{aligned}$$

$$M_p(r,\theta) = \sum_{n=0}^{\infty} A'_{nm} J_{n+\frac{1}{2}}\left(\frac{\varphi_{nm} r}{R}\right) \tag{45}$$

where

$$A'_{nm} = \sum_{m=0}^{\infty} A_{nm}\left[P_n^m(\cos\theta)\right] \tag{46}$$

Applying the results of Fourier series expansion of Bessel functions give [11, 17, 18]:

$$A'_{nm} = \frac{2}{R^2 J^2_{n+\frac{3}{2}}(\varphi_{nm})} \int_0^R r M_p(r,\theta) J_{n+\frac{1}{2}}\left(\frac{\varphi_{nm} r}{R}\right) \tag{47}$$

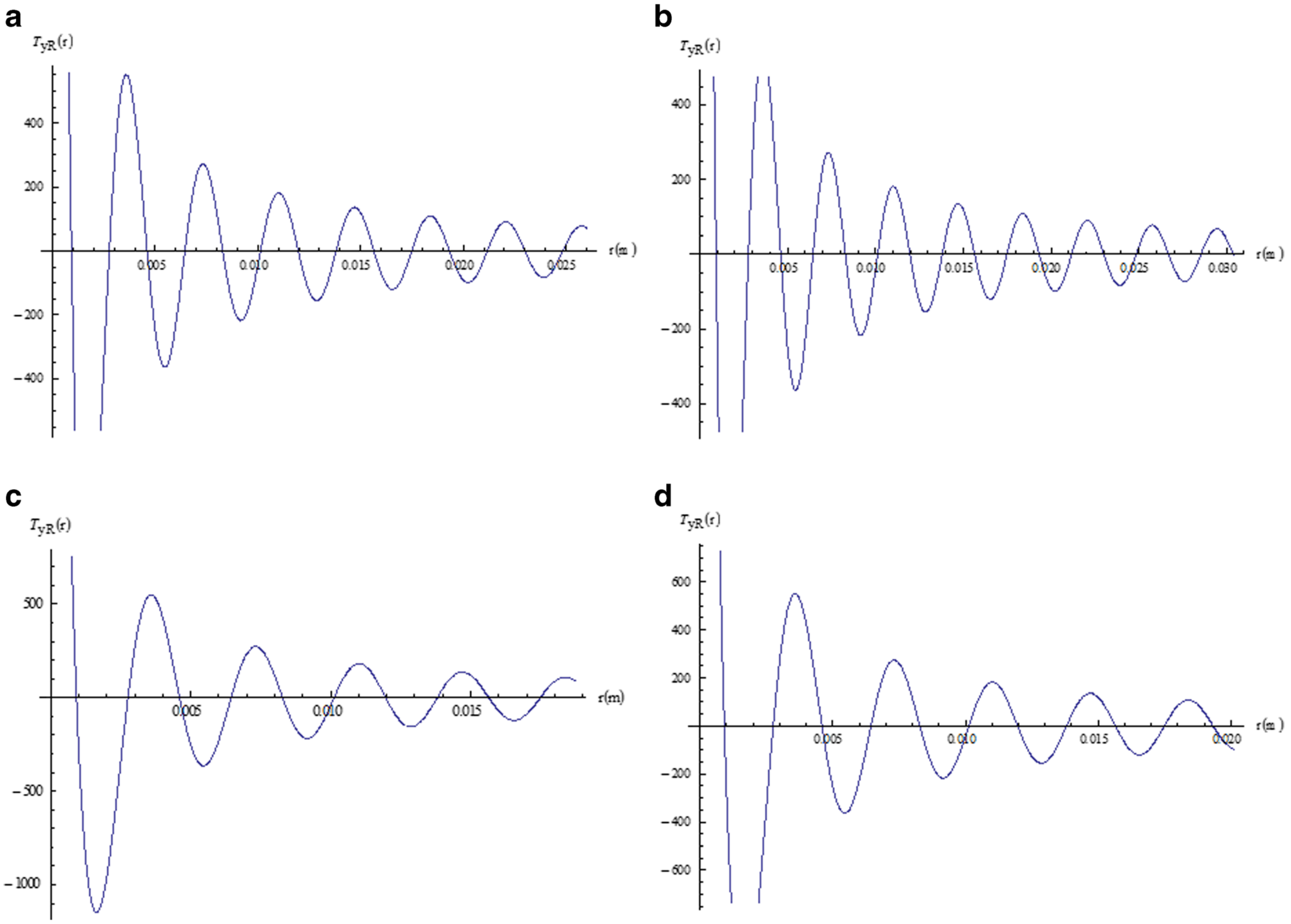

Fig. 1 Profiles of the tagging function applied to the left ventricle of the human heart for (**a**) female at diastole (**b**) male at diastole (**c**) female at systole (**d**) male at systole

Similarly, from Fourier series expansion of the associated Legendre polynomials, we derive from Eq. (47) as follows [17, 18]:

$$A_{nm} = \frac{2n+1}{2}\frac{(n+m)!}{(n+m)!}\int_0^{\pi} A'_{nm} P_n^m(\cos\theta)\sin\theta d\theta \tag{48}$$

The final solution of the diffusion NMR equation is therefore given as:

$$M_y(r,\theta,\phi,t) = \sum_{n=0}^{\infty}\sum_{m=0}^{\infty} A_{nm} J_{n+\frac{1}{2}}\left(\frac{\varphi_{nm} r}{R}\right) \tag{49}$$

$$\left[P_n^m(\cos\theta)\right][\sin m\varphi]e^{-\frac{\varphi_{nm}^2}{R^2}Dt - \frac{F_0\gamma g_r}{2DT_0}r^3}$$

For tagging MRI, we may write [19]:

$$r = \frac{m\pi}{2\gamma g\tau} \tag{50}$$

where γ is the gyromagnetic ratio, g is the gradient pulse magnitude and τ is the gradient pulse duration. Since $m = 0$, $1, 2, 3, \ldots\ldots$, we see that the expression of Eq. (49) is summing up all magnetization vectors for different values of m. If we make the following definition [20, 21]:

$$\lambda = \gamma g\tau \tag{51}$$

$$n = \frac{lT_1}{T_2} \tag{52}$$

where l is a dimensionless relaxation weighting parameter. Hence, if we set the parameter ϕ_{nm} as the phase at a fixed point r_0, we write:

$$\varphi_{nm} = \frac{m\pi}{2} = n\gamma g\tau r_0 \tag{53}$$

The NMR transverse magnetization becomes:

$$M_y(r,\theta,\phi,t) = \sum_n^{\infty}\sum_m^{\infty} A_{nm} J_{n+\frac{1}{2}}\left(n\gamma g\tau\frac{r_0}{R}r\right) \tag{54a}$$

$$\left(P_n^m(\cos\theta)\right)(\sin m\phi)e^{-\left(n\frac{\gamma g\tau r_0}{R}\right)^2 Dt - \frac{F_0\gamma g_r}{2DT_0}r^3}$$

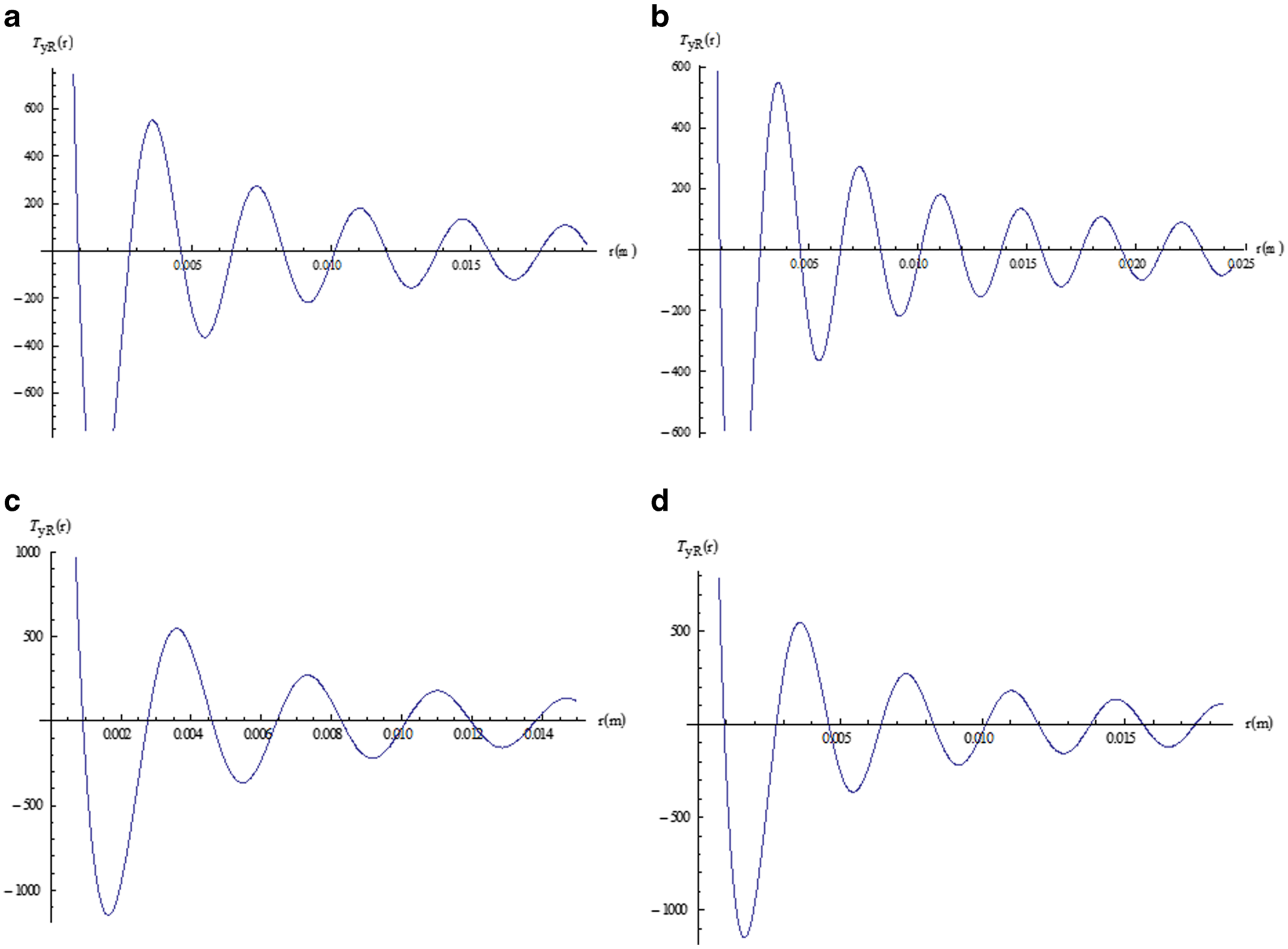

Fig. 2 Profiles of the tagging function applied to the right ventricle of the human heart for (**a**) female at diastole (**b**) male at diastole (**c**) female at systole (**d**) male at systole

Table 2 Myocardial diffusion coefficient and NMR relaxation times at 3.0 T taken from normal patients and patients with iron overload [24–26]

	Mid-diastole (Breath hold)	Mid-diastole (Free breathing)	End-systole (Breath hold)	Myocardial iron overload
T_1(s)	1.1565	1.1791	1.1426	1.1967
T_2(s)	0.0433	0.0447	0.0429	0.0470
D ($m^2\ s^{-1}$)	11.2×10^{-10}	11.2×10^{-10}	10.4×10^{-10}	9.8×10^{-10}

From Eq. (54a), the conventional diffusion b-factor [20, 21] is given as:

$$b = \left(n\frac{\gamma g \tau r_0}{R}\right)^2 t \tag{54b}$$

Radial tagging function

Due to the geometrical structure of the heart, the spherical wave equation from a point source could be used to describe the motion or vibration of the myocardium and concurrently carries the necessary information for tracking the diffusive spin within the heart's compartments. Since wave equation

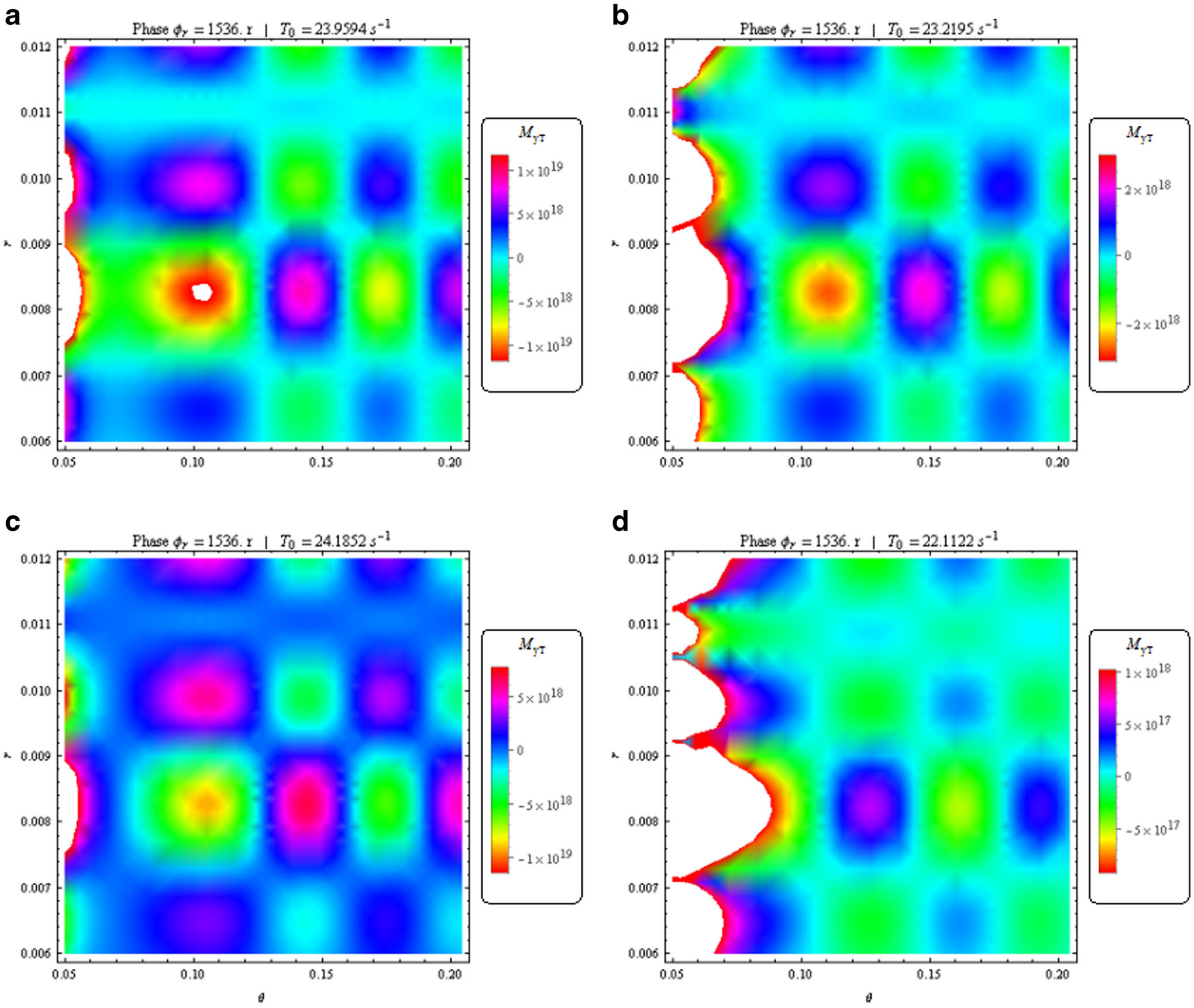

Fig. 3 Myocardial tagged images for (**a**) mid-diastole (breath hold) (**b**) mid-diastole (free breathing) (**c**) end-systole (breath hold) (**d**) myocardial iron overload

is not invariant under rotation of the spatial coordinates, we could seek for a solution with zero orbital angular momentum for this problem. It is assumed that the tagging gradients are applied in the radial direction. Therefore, the Laplacian operator

$$\nabla^2 = \frac{1}{r^2}\left(\frac{\partial}{\partial r}\left(r^2\frac{\partial}{\partial r}\right) + \frac{1}{\sin^2\theta}\frac{\partial^2}{\partial\phi^2} + \frac{1}{\sin\ \theta}\frac{\partial}{\partial\theta}\left(\sin\ \theta\frac{\partial}{\partial\theta}\right)\right) \quad (55)$$

reduces to a rotationally invariant form such that $\nabla^2 = \frac{1}{r^2}\left(\frac{\partial}{\partial r}\left(r^2\frac{\partial}{\partial r}\right)\right) = \frac{\partial^2}{\partial r^2} + \frac{2}{r}\frac{\partial}{\partial r}$.

It is possible to seek for solutions that depend only on the radial distance r, but not angular variables, from a given point. Such solutions then satisfy

$$\frac{\partial^2 T_y}{\partial t^2} - v_h^2\left(\frac{\partial^2 T_y}{\partial r^2} + \frac{2}{r}\frac{\partial T_y}{\partial r}\right) = 0 \quad (56)$$

where v_h represents the speed of vibration of the myocardium. Eq. (56) may then be written as:

$$\frac{\partial^2 (rT_y)}{\partial t^2} - v_h^2\frac{\partial^2 (rT_y)}{\partial r^2} = 0 \quad (57)$$

The quantity $rT_y(r, t)$ in Eq. (57) satisfies the one-dimensional wave equation with no forcing function (i.e. freely vibrating myocardial motion). If we again restrict our solution to spherical waves that oscillate in time with well-defined angular frequency ω (Larmor frequency), then the transformed tagging function $rT_y(r, t)$ has simple plane wave solutions

$$T_y(r, t) = \frac{A}{r}e^{i(\omega t \pm \lambda r)} \quad (58)$$

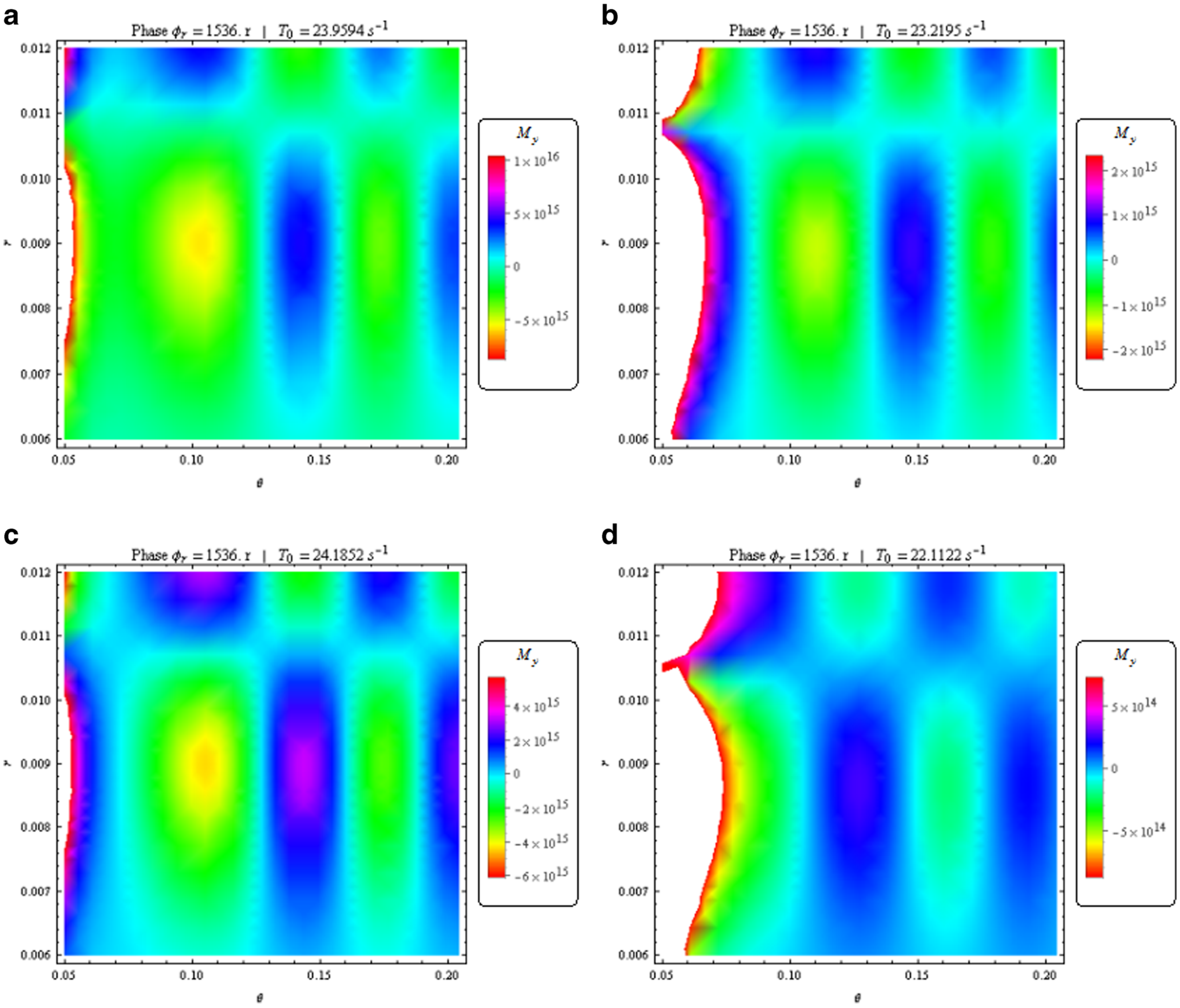

Fig. 4 Myocardial untagged images for (**a**) mid-diastole (breath hold) (**b**) mid-diastole (free breathing) (**c**) end-systole (breath hold) (**d**) myocardial iron overload

At a reference time $t = 0$, Eq. (58) becomes

$$T_y(r) = \frac{A}{r} e^{i(\pm \lambda r)} \tag{59}$$

Eq. (59) is a complex tagging function in polar coordinate for gradient applied in the radial direction. The ± signs indicate the tagging gradient directions (both directions), λr represent the tagging phase. The constant λ is known as the spatial tagging frequency which defines how many revolutions in a unit length scale. This is similar to the angular frequency ω function in time domain that defines how many revolutions in a unit time:

$$\lambda = \frac{\omega}{v} = \gamma g \tau \tag{60}$$

where γ is the gyromagnetic ratio, g is the magnitude of the tagging gradient pulse and τ is the pulse duration. These parameters are linked through the propagation velocity v, which can be determined from the physical properties of the media through which the wave travels. The complex tagging function can be broken into real and imaginary part as shown in Eq. (61)

$$T_y(r) = \frac{A}{r} \left(\cos(\pm \gamma g \tau) r + i \sin(\pm \gamma g \tau) r \right) \tag{61}$$

The real component of the tagging function which quantifies the magnitude of the harmonic image is

$$T_{yR}(r) = \frac{A}{r} \cos(\pm \gamma g \tau) r \tag{62}$$

The imaginary part of Eq. (60) describes the harmonic phase magnetization as

$$T_{yI}(r) = \frac{A}{r} i \sin(\pm \gamma g \tau) r \tag{63}$$

Tagged magnetization for cardiac imaging

Since the tagged magnetic resonance function $M_{yT}\left(\overrightarrow{r}, t\right)$ is stated analytically as the combination of anatomy function and tagging function, we can write:

$$M_{yT}\left(\overrightarrow{r}, t\right) = M_y\left(\overrightarrow{r}, t\right) T_y(r) \tag{64}$$

This is given by Eq. (54) and any of Eqs. (59), (62), (63) depending on what is being achieved as:

$$M_{yT}(r, \theta, \phi, t) = \left(\frac{A}{r} e^{i(\pm \lambda r)} \right) \left(\sum_{n}^{\infty} \sum_{m}^{\infty} A_{nm} J_{n+\frac{1}{2}} \left(n \gamma g \tau \frac{r_0}{R} r \right) \left(P_n^m(\cos\theta) \right) (\sin m\phi) e^{-\left(n \frac{\gamma g \tau r_0}{R} \right)^2 Dt - \frac{F_0 \gamma g_r}{2DT_0} r^3} \right) \tag{65}$$

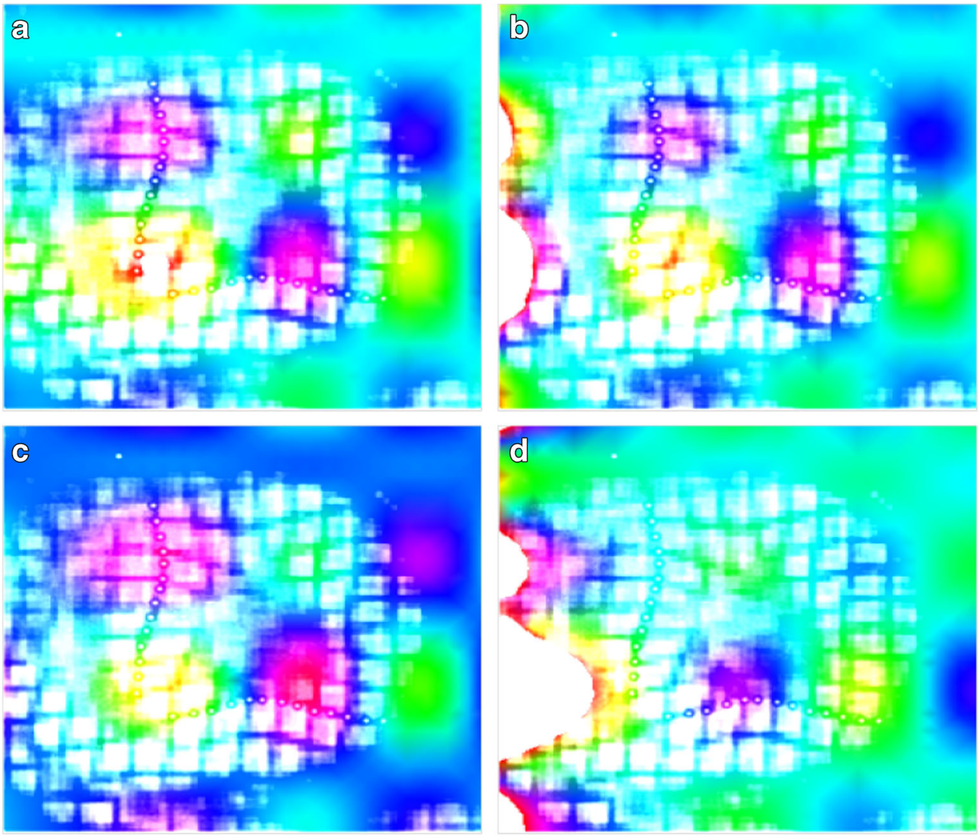

Fig. 5 Myocardial tagged images superimposed on cardiac MRI slice for (**a**) mid-diastole (breath hold) (**b**) mid-diastole (free breathing) (**c**) end-systole (breath hold) (**d**) myocardial iron overload

Eq. (65) describes the time series distribution of magnetic resonance transverse magnetization over radial distance, and can be used to track material point along the myocardium radius. For the purpose of computer code development, it is important to state the parameters available for the program. These are: tissue relaxation time ratio $n = l\frac{T_1}{T_2}$, harmonic image constant $m \geq l\frac{T_1}{T_2}$, diffusion coefficient D, relaxation rate $T_0 = \frac{T_1+T_2}{T_1 T_2}$, reference approximate myocardial radius R, pulse duration τ and gradient pulse magnitude g.

Analysis of results

The tagging function visualization and it implication is very important according to Eq. (61). A Wolfram Mathematica computer has been developed to simulate the behaviour of this function for cardiac imaging. In order to demonstrate the use of the computer program, we have made use of normal cardiac radial measurements of the human heart [22]. These measurements are gender based and are presented in Table 1.

Using the information in Table 1, profiles of the tagging function from the graphic user interface (GUI) are given in Figs. 1 and 2 (the parameters used are A = 1, g = 0.02 T/m and τ = 2 ms):

In Figs. 1 and 2, the profiles showed that the real component of the tagging function varies uniquely with myocardium radial distance during the systole and diastole. In addition to this, the tagging wave magnitude and attenuation are gender dependent. These profiles showed that Eq. (62) is quite useful in visualizing the real tagging component function for different regions of the heart as long as their radial extents are quantifiable. However, we have introduced a radial adjustment parameter in the computer program for flexibility such that users could adapt the program for any heart region and types of measurements such that new codes are not required for any changes.

Initially, the tags remain visible over short distances before decaying. This attenuation is known as “tag fading”, a phenomenon that occurs during myocardial tissue displacement [19, 23]. The amplitude factor *A* in Eq. (62) may be chosen in such a way that the tag fading is minimized as the procedure of cardiac imaging requires. In addition to this, NMR relaxation could be introduced into the tagging function so that the tag

Table 3 Computed displacements and radial strains as a function of time and deformed radius during mid-diastole (Breath hold) [T_1 = 1.1565s, T_2 = 0.0433 s]

Time, t(s)	Radius, r(m)	Reference radius, R_0(m)	Displacement, u	Radial strain, ε_r
0	0.0063	−0.01124	0.017544	−1.56032
0.0335	0.0067	−0.00487	0.011566	−2.37681
0.067	0.0069	−0.00344	0.010338	−3.00725
0.1005	0.0071	−0.00195	0.009051	−4.63879
0.134	0.0075	0.00734	0.00016	0.021866
0.1675	0.0079	0.011777	−0.00388	−0.32922
0.201	0.0081	0.011773	−0.00367	−0.31200
0.2345	0.0082	0.011655	−0.00345	−0.29642
0.268	0.0087	0.006032	0.002668	0.442391
0.3015	0.0091	−0.0035	0.012597	−3.60224
0.335	0.0092	−0.0009	0.010101	−11.2151
0.3685	0.0095	−0.00627	0.015766	−2.51601
0.402	0.0097	−0.00751	0.017205	−2.29247
0.4355	0.0103	−0.00929	0.019594	−2.10825
0.469	0.0105	−0.00828	0.018777	−2.26852
0.5025	0.0107	−0.00712	0.017822	−2.50236
0.536	0.0113	0.009224	0.002076	0.225092
0.5695	0.0115	0.010097	0.001403	0.138969
0.603	0.0117	0.010801	0.000899	0.083247
0.6365	0.012	0.011772	0.000228	0.019373
0.67	0.0121	0.011658	0.000442	0.037948
0.701	0.0123	0.011798	0.000502	0.042526
0.725	0.0125	0.011235	0.001265	0.11258
0.773	0.0128	0.010098	0.002702	0.267553
0.8	0.013	0.008343	0.004657	0.558127

fading reflects information on disease state of myocardium cells since the protons associated with such cells are capable of absorbing RF pulses used to tag the heart.

The behaviour of the cardiac magnetic resonance signal for both untagged and tagged anatomy components of the NMR transverse magnetization are given by Eqs. (54a) and (65) respectively. Wolfram Mathematica computer programs have been developed based on these expressions and the resulting myocardial images have been obtained with the use of experimental data. The experimental data are the mean diffusivity (at systole and diastole) [24], T_1 and T_2 relaxation times [25, 26] measured at 3.0 T (for mid-diastole during breath hold, mid-diastole during free breathing, end-systole during breath hold and patients with iron overload [26]). The mean diffusion coefficients (taken to represent D in this study) used for imaging were those taken from the apex of the myocardium [24]. These data are presented in Table 2.

The execution of the computer program and the values in Table 2, we have the images in Figs. 3, 4, and 5.

Data flexibility has been incorporated in the development of the computer programs. Appropriate and diverse parameters can easily be inserted in the input fields in order to obtain interesting myocardial images and this has facilitated the images in Figs. 3 and 4. The beauty of these programs is in their compatibility with any type or combination of imaging/relaxation data. In addition to this, reference and fixed values of the endocardium radial measurements can easily be changed as the clinical situation requires.

As demonstrated in Figs. 3 and 4, this model is not only useful for imaging different phases of the cardiac cycle but also able to detect disease conditions of the heart. Myocardial iron overload, ensuing dilatation and heart failure are the main causes of death in patients with primary and secondary forms of hemochromatosis [26] and we have demonstrated that this medical problem showed the least MR signal (for both tagged and untagged images) as compared to normal systolic and diastolic cardiac motions. This is shown in Figs. 3d and 4d, where it would be observed that the myocardial iron overload has a unique MR signal distribution, which is most pronounced around the points $r = 7$ mm and 9 mm. Also, at low values of the radial point orientation θ (around 0.075 rad), the MR signal is complex and this may be due to the presence of bifurcations or myocardial regions from which blood has just been emptied. The reason for the latter possibility is the absence of significant amount of blood protons available for the production of measurable level of transverse magnetization M_y.

Table 4 Computed displacements and radial strains as a function of time and deformed radius during mid-diastole (Free breathing) [$T_1 = 1.1791$s, $T_2 = 0.0447$ s]

Time, t(s)	Radius, r(m)	Reference radius, R_0(m)	Displacement, u	Radial strain, ε_r
0	0.0063	−0.00868	0.014981	−1.72569
0.0335	0.0067	0.000666	0.006034	9.060936
0.067	0.0069	0.002551	0.004349	1.704893
0.1005	0.0071	0.00437	0.00273	0.624868
0.134	0.0075	0.011244	−0.00374	−0.33296
0.1675	0.0079	0.009903	−0.002	−0.20226
0.201	0.0081	0.008743	−0.00064	−0.07353
0.2345	0.0082	0.01014	−0.00194	−0.19129
0.268	0.0087	−0.00246	0.011162	−4.53387
0.3015	0.0091	−0.01048	0.019581	−1.86828
0.335	0.0092	−0.0092	0.018399	−2.00016
0.3685	0.0095	−0.01166	0.021159	−1.8148
0.402	0.0097	−0.0118	0.0215	−1.82205
0.4355	0.0103	0.000484	0.009816	20.28442
0.469	0.0105	0.002373	0.008127	3.425326
0.5025	0.0107	0.0042	0.0065	1.547747
0.536	0.0113	0.010878	0.000422	0.03884
0.5695	0.0115	0.010001	0.001499	0.149895
0.603	0.0117	0.008864	0.002836	0.31991
0.6365	0.012	0.003797	0.008203	2.160686
0.67	0.0121	0.005935	0.006165	1.038785
0.701	0.0123	0.003754	0.008546	2.276449
0.725	0.0125	4.06E-05	0.012459	307.2472
0.773	0.0128	−0.00322	0.01602	−4.97568
0.8	0.013	−0.00613	0.019132	−3.11986

Meanwhile, in order to simulate the algorithm for clinical images, we have superimposed the tagged images in Fig. 2 over a selected cardiac MRI slice and presented the results in Fig. 5. As demonstrated in these images, the methods developed in this study is not only good for anatomical imaging (Fig. 5a–c) but also in the diagnosis of cardiac disease conditions (Fig. 5(a,b,c) vs (d)). In addition to these, the colour-coded images could prove to be an upgrade on the normal gray scale images because of their ability to delineate tissue information that are suppressed in the contemporary image sequences.

Tagging and encoding cardiac tissue motion

Magnetic resonance tagging makes use of a unique pulse sequence to spatially modulate the longitudinal magnetization of cardiac tissues before the acquisition of image data [27, 28]. From here, a lot of image data can be acquired in order to perform image reconstruction and this is achieved over many heartbeats within a single breath hold. The reconstructed images are reflective of MR tag pattern deformations due to the underlying motion of the heart [28]. Despite the significant improvements made in MR tagged image acquisition methods, these methods still suffer from lack of fast quantitative analysis and visualization techniques. This challenge is hindering the wide application of MR tagging in clinical settings.

The existing methods of MR tagging analysis have downsides, which involve the use of manual intervention in feature detections [29, 30]. There are currently attempts in automating feature detection but it is still proving very difficult [31]. Furthermore, since image features have to be distinct, dense motion estimation would always require interpolation. Lastly, since epicardial and endocardial boundaries of the left ventricle are generally used for feature interpolation process, modifications involving motion estimation in the right ventricle may require new cardiac modelling and software for visualization [27]. Hence, the current methods are cumbersome and time consuming because the requirements of manual intervention and numerous interpolations; these problems are significant hindrance to their use for real-time diagnosis.

Most techniques for motion analysis in MR tagging rely largely on image-processing approaches that are able to detect tag features, which are then combined into a detailed motion map (displacement and/or strain) using interpolation [27].

Table 5 Computed displacements and radial strains as a function of time and deformed radius during end-systole (Breath hold) [$T_1 = 1.1426$s, $T_2 = 0.0429$ s]

Time, t(s)	Radius, r(m)	Reference radius, R_0(m)	Displacement, u	Radial strain, ε_r
0	0.0063	−0.01179	0.01809	−1.53433
0.0335	0.0067	−0.00774	0.014441	−1.86553
0.067	0.0069	−0.00666	0.013562	−2.0357
0.1005	0.0071	−0.00549	0.012594	−2.29221
0.134	0.0075	0.003831	0.003669	0.957771
0.1675	0.0079	0.010749	−0.00285	−0.26508
0.201	0.0081	0.011239	−0.00314	−0.2793
0.2345	0.0082	0.010098	−0.0019	−0.18799
0.268	0.0087	0.009597	−0.0009	−0.09346
0.3015	0.0091	0.001586	0.007514	4.73821
0.335	0.0092	0.004255	0.004945	1.162042
0.3685	0.0095	−0.00114	0.010635	−9.36765
0.402	0.0097	−0.00248	0.012182	−4.9077
0.4355	0.0103	−0.01166	0.021958	−1.88355
0.469	0.0105	−0.01137	0.021869	−1.92357
0.5025	0.0107	−0.01093	0.021629	−1.97908
0.536	0.0113	0.003827	0.007473	1.952423
0.5695	0.0115	0.005089	0.006411	1.259732
0.603	0.0117	0.006283	0.005417	0.862191
0.6365	0.012	0.010097	0.001903	0.188528
0.67	0.0121	0.008404	0.003696	0.439752
0.701	0.0123	0.009611	0.002689	0.279821
0.725	0.0125	0.011133	0.001367	0.12279
0.773	0.0128	0.011708	0.001092	0.093311
0.8	0.013	0.011737	0.001263	0.107635

Consequently, our computational approach to address the problems highlighted above is based on displacement-strain analyses. From current methods, the displacement field in the cardiac tissues is given as [19, 23, 27]:

$$u\left(\overrightarrow{r},t\right)=\overrightarrow{r}-p\left(\overrightarrow{r},t\right) \tag{66}$$

where $\overrightarrow{r}$ represents the current tissue position and $p\left(\overrightarrow{r},t\right)$ is the reference position. Considering only radial displacements, we could now modify Eq. (66) as follows:

$$u(r,t)=r-R\cos\left[\left(n\frac{T_2 r_0}{\delta\ R}\gamma g\tau\right)r-\left(n\frac{\tau}{T_1}\gamma gR\right)t\right] \tag{67}$$

where $n\gamma g\frac{r_0}{R}r$ is the tagging angular frequency as extracted from Eq. (54a), τ is the tagged pulse duration, g is the tagging gradient field, $n=\frac{lT_1}{T_2}$ and l is as defined in earlier sections. Equation (67) then becomes:

$$u(r,t)=r-R\cos\left[\left(l\frac{r_0}{R}\gamma gT_1\right)r-\left(l\frac{\tau}{T_2}\gamma gR\right)t\right] \tag{68}$$

The choice of the function in Eq. (67) is based on a straightforward association of reference points with magnetic resonance relaxations and cardiac cycle so that displacements at any point within the cardiac cycle could be mapped to different cardiac disease conditions. This could provide a new dimension to current research efforts [32, 33] employing strain analysis in tissue diagnosis. The reference position is therefore no longer constant but given as:

$$p(r,t)=R\cos\left[\left(l\frac{r_0}{R}\gamma gT_1\right)r-\left(l\frac{\tau}{T_2}\gamma gR\right)t\right] \tag{68}$$

We now define the relaxation-dependent reference position as

$$R_0=R\cos\left[\left(l\frac{r_0}{R}\gamma gT_1\right)r-\left(l\frac{\tau}{T_2}\gamma gR\right)t\right] \tag{69}$$

Meanwhile, at time $t=0$ (end-diastole), the myocardial point $r=\frac{\pi}{2}$ gives:

$$p=R;u=\frac{\pi}{2}-R$$

Table 6 Computed displacements and radial strains as a function of time and deformed radius during myocardial iron overload [T_1 = 1.1967s, T_2 = 0.0470 s]

Time, t(s)	Radius, r(m)	Reference radius, R_0(m)	Displacement, u	Radial strain, ε_r
0	0.0063	−0.00553	0.011826	−2.14009
0.0335	0.0067	0.005077	0.001623	0.319626
0.067	0.0069	0.007089	−0.00019	−0.02662
0.1005	0.0071	0.008819	−0.00172	−0.19488
0.134	0.0075	0.011552	−0.00405	−0.35076
0.1675	0.0079	0.004954	0.002946	0.594757
0.201	0.0081	0.002732	0.005368	1.965364
0.2345	0.0082	0.004598	0.003602	0.783484
0.268	0.0087	−0.00923	0.01793	−1.94259
0.3015	0.0091	−0.0114	0.020505	−1.79791
0.335	0.0092	−0.01175	0.020949	−1.78304
0.3685	0.0095	−0.00933	0.018831	−2.01815
0.402	0.0097	−0.00771	0.017413	−2.25764
0.4355	0.0103	0.009614	0.000686	0.071342
0.469	0.0105	0.01078	−0.00028	−0.02597
0.5025	0.0107	0.011518	−0.00082	−0.07098
0.536	0.0113	0.001475	0.009825	6.659803
0.5695	0.0115	−0.00088	0.012376	−14.1323
0.603	0.0117	−0.00319	0.014892	−4.66557
0.6365	0.012	−0.00879	0.020785	−2.36593
0.67	0.0121	−0.00736	0.019457	−2.64472
0.701	0.0123	−0.00933	0.021635	−2.31767
0.725	0.0125	−0.01125	0.023747	−2.11145
0.773	0.0128	−0.0118	0.024595	−2.08516
0.8	0.013	−0.01116	0.02416	−2.16484

In order to estimate the mechanical deformation of cardiac tissues, we define the endocardial radial strain (ε_r) as follows [19, 34, 35]:

$$\varepsilon_r = \frac{R-R_0}{R_0} \tag{70}$$

In order to adequately diagnose and manage ischemic heart diseases, echocardiographic assessment of regional myocardial function is required. However, this method depends on visual detection of motion of myocardium as well as the assessment of left ventricular ejection fraction [35], a technique which is plagued with numerous challenges. Newer indices involving myocardial strain and strain rate analysis are now being used in order to overcome these challenges. Displacements and strains have been able to quantify myocardial deformations (taking place at systole and diastole). Deformation abnormalities are often noticed in early onsets of many patho-physiological conditions such as ischemia. Consequently, these deformations provide means of delineating regional myocardial dysfunction. Although displacement and strain estimation have been applied widely to cardiac mapping and diagnosis, the unique relaxation (T_1 and T_2) parameters, which are excellent indicators of tissue diseases, have not been fully explored for better diagnosis of heart diseases, monitoring of disease progression and treatment outcomes. Fortunately, the definitions provided in Eqs. (67) to (70) could provide a completely new dimension to cardiac tissue displacement and strain analysis.

In order to demonstrate the importance of the methods , we shall make use of the data in Table 2 to make computations of the displacements and strains at different points within the cardiac cycle. Normal cardiac tissue condition are represented as mid-diastole (Breath hold), mid-diastole (Free breathing) and end-systole (Breath hold) while myocardial iron overload condition has been selected to represent a myocardial

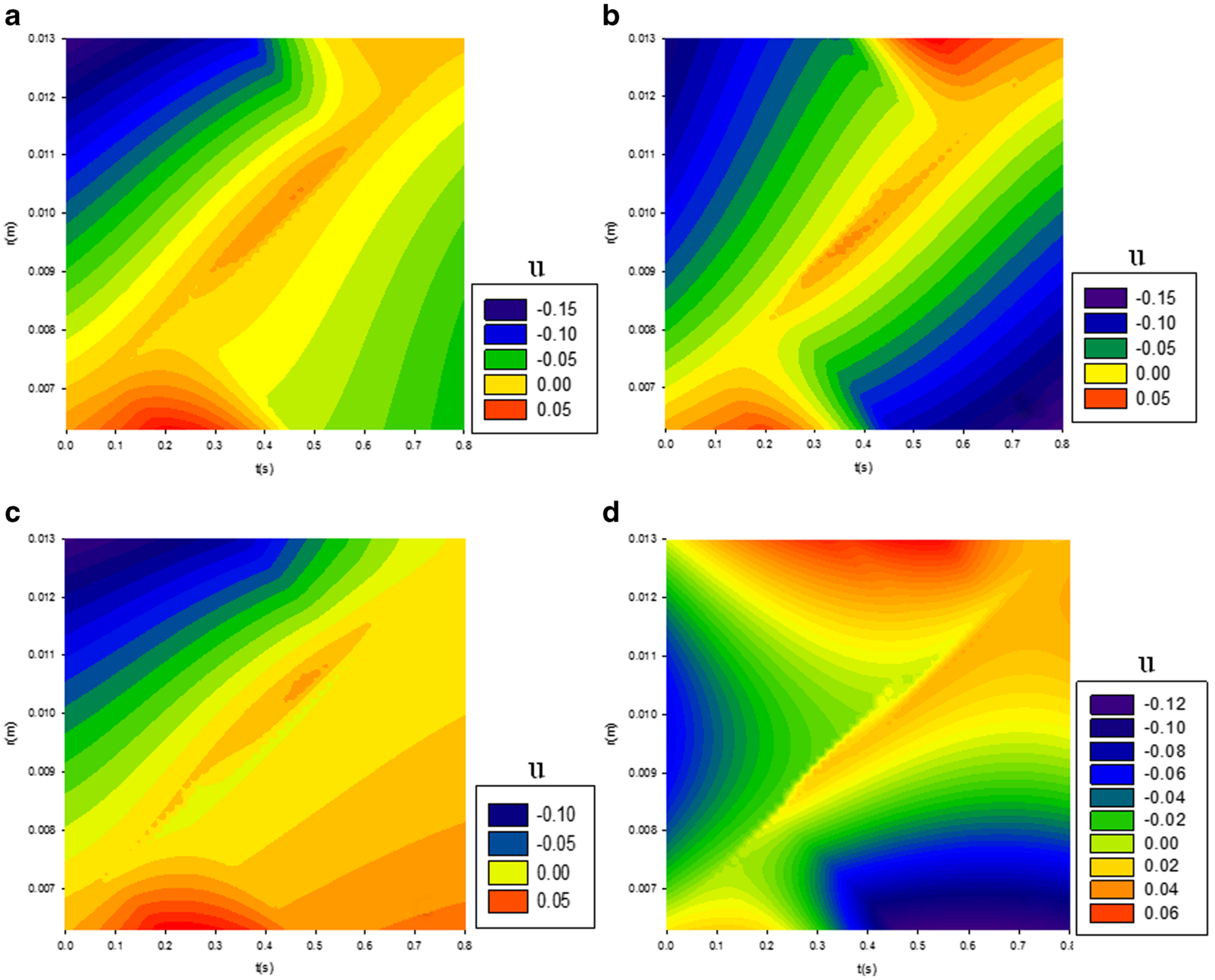

Fig. 6 Radial displacement as a function of time and deformed radius at (**a**) mid-diastole (Breath hold) (**b**) mid-diastole (Free breathing) (**c**) end-systole (Breath hold) (**d**) myocardial iron overload

dysfunction. As a first step in achieving this, we have mapped deformed endocardial radii of 0.0063 m - 0.013 m to various points within the cardiac cycle. The values of the constant parameters used for computations of Tables 3, 4, 5 and 6 are $l = 0.04125$, $g = 0.018\,\mathrm{T\,m^{-1}}$, $\tau = 2$ ms, $\gamma = 42{,}666{,}666.67\ \mathrm{s^{-1}\,T^{-1}}$, $r_0 = 0.00114$ m and $R = 0.0118$ m.

Using the computations in Tables 3 to 6, we have obtained distribution maps of displacement and radial strain for the normal and abnormal heart condition in Figs. 6 and 7.

Figures. 6 and 7 demonstrated that the computed displacements and radial strains are distributed in such a way that their values showed contrast between different normal conditions. The significance of this is in early detection of myocardial dysfunction and in monitoring disease progression. Since the methods developed are able to differentiate different normal cardiac conditions, they would definitely be very good for improved diagnosis. The importance of this to disease diagnosis is shown in Figs. 6d and 7d where the contrast is conspicuous. It is also interesting to note that radial strain tends to be better in diagnosis than the use of displacement. This is especially obvious in Fig. 6a and 6c where there is no significant difference in the displacement distribution of mid-diastole (Breath hold) and end-systole (Breath hold). Meanwhile, Fig. 7a and 7c demonstrated that radial strain distribution is better in showing difference between these conditions. Generally, the image contrasts in Fig. 7 are better than those of Fig. 9. However, displacement distribution tend to be better in mapping heart condition at mid-diastole (Free breathing and at the beginning of the cardiac cycle) and myocardial iron overload towards the end of the cardiac cycle (shown in Fig. 6b and 6d as compared to Fig. 7b and 7d). The implication of this could be that for myocardial conditions which are directly related to cardiac cycle, displacement distribution could be more reliable compared to radial strain analysis. In addition to the computational approach used in this analysis which is fast, cost-effective and less-cumbersome, we can employ this method to interpolate for displacements or radial strains for inaccessible deformed radial measurements.

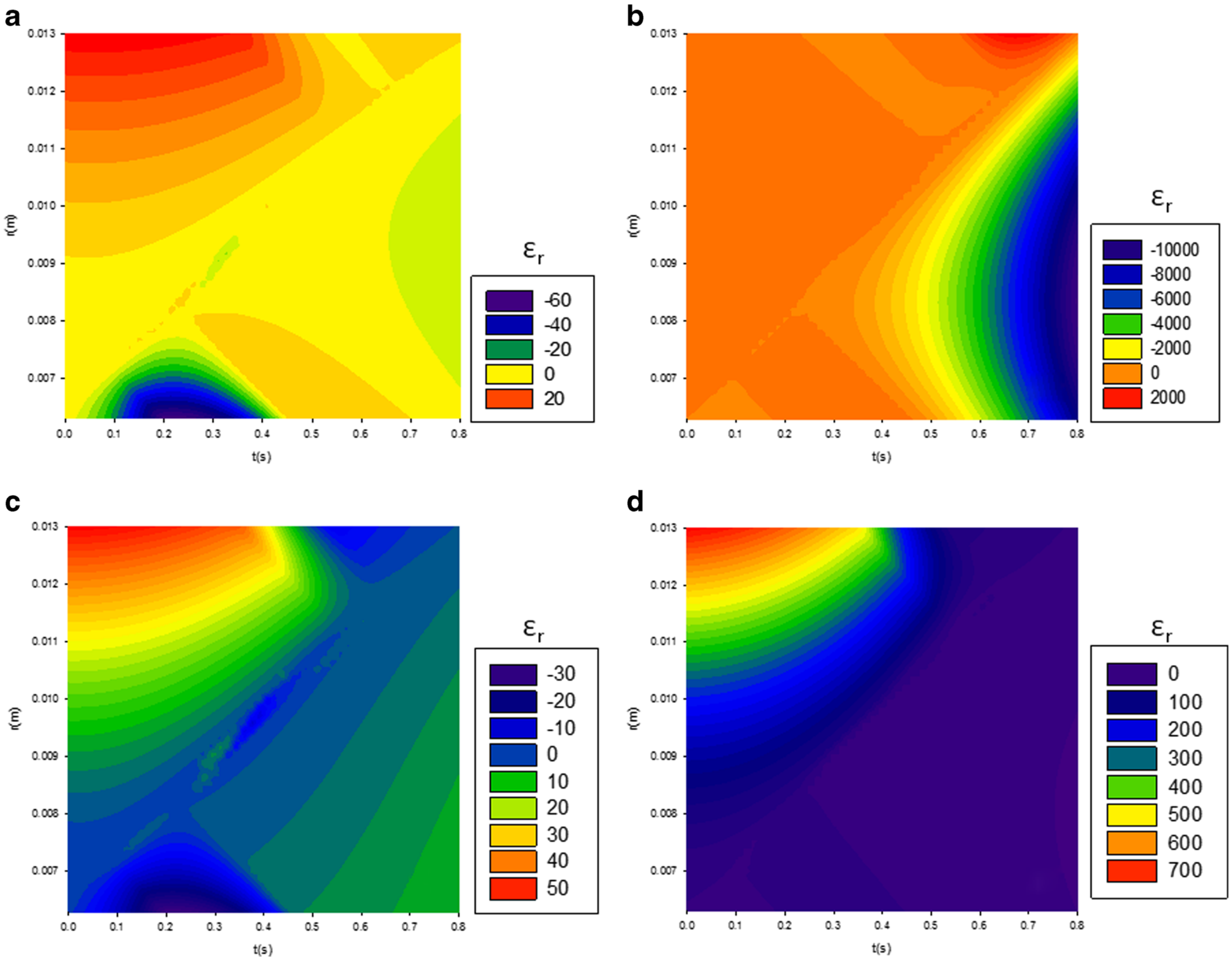

Fig. 7 Radial strain as a function of time and deformed radius at (**a**) mid-diastole (Breath hold) (**b**) mid-diastole (Free breathing) (**c**) end-systole (Breath hold) (**d**) myocardial iron overload

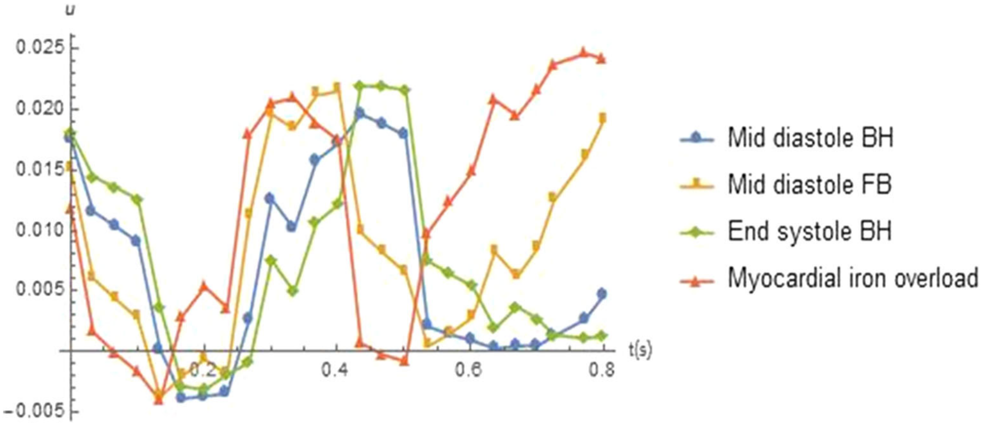

Fig. 8 Multiple plots of radial displacement against the time at mid-diastole (Breath hold-BH), mid-diastole (Free breathing-FB), end-systole (Breath hold-BH) and myocardial iron overload

Figures 8 and 9 further elucidate the behaviour of displacement and radial strain as functions of time.

As shown in Fig. 8, at mid-diastole (Free breathing-FB) and myocardial iron overload, the displacements are low just at the onset of the cardiac cycle and have the highest values towards the end of the cycle. Hence, if the displacement is to be sampled for any diagnostic reason, the appropriate times for best measurements have thus been demonstrated. This could be very important in relating the measured displacement to the blood pumping process of the heart. Fig. 9 is more complicated because of the data distribution within the profile. The best time for sampling radial strain for dysfunction (myocardial iron overload) is around 0.2 s where the strain for normal conditions are not far from zero. This may prove to be very important for monitoring disease progression because the curves would tend to evolve differently at different points within the cardiac cycle. In addition to this, we could use these profiles to monitor how a patient suffering from myocardial dysfunction is responding to treatment. However, in such cases, the profile evolution needs to be automated so that patients' condition could be observed in real time.

Conclusion

We have developed detailed analytical solution to the Bloch NMR flow equation for myocardial tagging function using spherical wave model with spin diffusion. The systolic and diastolic functions of the heart are mathematically simulated using diffusive magnetization distribution. This will be a useful tool to investigate mechanical factors involved in normal and abnormal cardiac function or to aid in the design and evaluation of new therapies for impaired cardiac function. Based on the newly developed spherical wave tagging function for myocardial motion, Harmonic Phase MRI method was used to compute the difference between tagged and untagged magnetization. It is interesting to note that we used the less-elusive transverse magnetization instead of the longitudinal magnetization (M_z) function. The limitation of conventional cardiac function measurements is the inability to follow the motion of individual portions of the heart wall during RF excitations and the onset of Fourier induction decay (FID). The computational HARP-MRI as presented in this investigation may measure myocardial motion and strain in near real-time and may be seen as a potential candidate to make Magnetic Resonance Tagging clinically viable. It can

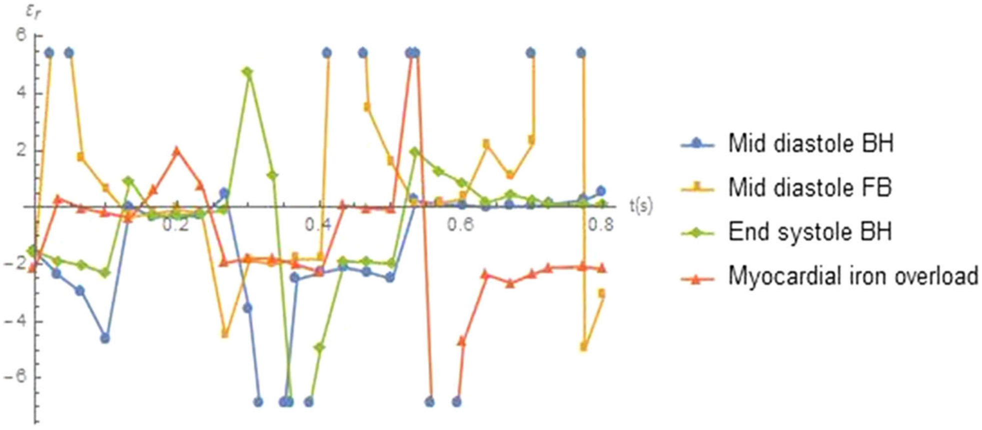

Fig. 9 Multiple plots of radial strain against the time at mid-diastole (Breath hold-BH), mid-diastole (Free breathing-FB), end-systole (Breath hold-BH) and myocardial iron overload

significantly allow for accurate monitoring and forecast in clinical settings using computer programming before and after the actual commencement of specific medical procedure for diagnosis and therapy.

References

1. Moore, C.C., McVeigh, E.R., and Zerhouni, E.A., Noninvasive measurement of three-dimensional myocardial deformation with tagged magnetic resonance imaging during graded local ischemia. *J. Cardiovasc. Magn. Reson.* 1(3):207–222, 1999. https://doi.org/10.3109/10976649909088333.
2. Dawson, J., and Lauterbur, P.C., Magnetic resonance imaging. *Scholarpedia*. 3(7):3381, revision #123947, 2008. https://doi.org/10.4249/scholarpedia.3381.
3. Edvardsen, T., Rosen, B.D., Pan, L., Jerosch-Herold, M., Lai, S., Hundley, W.G., Sinha, S., Kronmal, R.A., Bluemke, D.A., and Lima, J.A., Regional diastolic dysfunction in individuals with left ventricular hypertrophy measured by tagged magnetic resonance imaging-the multi-ethnic study of atherosclerosis (MESA). *Am. Heart J.* 151(1):109–114, 2006. https://doi.org/10.1016/j.ahj.2005.02.018.
4. Baer, T., Gore, J.C., Boyce, S., and Nye, P.W., Application of MRI to the analysis of speech production. *Magn. Reson. Imaging*. 5(1):1–7, 1987. https://doi.org/10.1016/0730-725X(87)90477-2.
5. Juliane, A., Mobile NMR for rock porosity and permeability. Dissertation. RWTH Aachen University, Aachen, Germany, 2007.
6. Rieu, R., In vivo study of physiological type flow in a bifurcation vascular prosthesis. *J. Biomech.* 24(10):923–933, 1991. https://doi.org/10.1016/0021-9290(91)90170-R.
7. Vogt, S. J., Nuclear magnetic resonance studies of biological and biogeochemical processes. Dissertation, Montana State University-Bozeman, 2013.
8. Awojoyogbe, O.B., A mathematical model of Bloch NMR equations for quantitative analysis of blood flow in blood vessels of changing cross-section I. *Physica A*. 303:163–175, 2002. https://doi.org/10.1016/S0378-4371(01)00379-X.
9. Awojoyogbe, O.B., A mathematical model of Bloch NMR equations for quantitative analysis of blood flow in blood vessels with changing cross-section II. *Physica A*. 323:534–550, 2003. https://doi.org/10.1016/S0378-4371(02)02025-3.
10. Awojoyogbe, O.B., Analytical solution of the time-dependent Bloch NMR flow equations: A translational mechanical analysis. *Physica A*. 339(3):437–460, 2004. https://doi.org/10.1016/j.physa.2004.03.061.
11. Awojoyogbe, O.B., Dada, O.M., Faromika, O.P., and Dada, O.E., Mathematical concept of the Bloch flow equations for general magnetic resonance imaging: A review. *Concepts Magn Reson A*. 38(3):85–101, 2011. https://doi.org/10.1002/cmr.a.20210.
12. Gupta, A., Stait-Gardner, T., Ghadirian, B., Price, W.S., Dada, O.M., and Awojoyogbe, O.B., *Theory, dynamics and applications of MR imaging-I*. Science PG, New York, 2014.
13. Awojoyogbe, O.B., Dada, O.M., Onwu, O.S., Ige, A.T., and Akinwande, I.N., Computational diffusion magnetic resonance imaging based on time-dependent Bloch NMR flow equation and Bessel functions. *J. Med. Syst.* 40:106, 2016. https://doi.org/10.1007/s10916-016-0450-4.
14. Dada, O.M., Awojoyogbe, O.B., and Ukoha, A.C., A computational analysis for quantitative evaluation of petrol-physical properties of rock fluids based on Bloch NMR diffusion model for porous media. *J. Pet. Sci. Eng.* 127:137–147, 2015. https://doi.org/10.1016/j.petrol.2015.01.003.
15. Spiegel, M.R., *Schaum's outline series of theory and problems of advanced mathematics for engineers and scientists*. McGraw-Hill, Singapore, 1983.
16. Cowan, B.P., *Nuclear magnetic resonance and relaxation*, 1st edn. Cambridge University Press, Cambridge, 1997.
17. Wylie, C.R., and Barrett, C.L., *Advanced engineering mathematics*, 5th edn. McGrawl – Hill, Tokyo, 1982.
18. Kreyszig, E., *Advanced engineering mathematics*, 7th edn. John Wiley and Sons, Singapore, 1996.
19. Parthasarathy, V., Characterization of harmonic phase MRI: theory, simulations, and applications. Dissertation, The John Hopkins University, 2006.
20. Price, W.S., Pulsed-field gradient NMR as a tool for studying translational diffusion. Part I. Basic theory. *Concepts Magn Reson*. 9:299–336, 1997. https://doi.org/10.1002/(SICI)1099-0534(1997)9:5<299::AID-CMR2>3.0.CO;2-U.
21. Price, W.S., *NMR studies of translational motion*. Cambridge University Press, Cambridge, 2009.
22. Hergan, K., Schuster, A., Mair, M., Burger, R., and Töpker, M., Normal cardiac diameters in cine-MRI of the heart. *RoFo*. 176(11):1599–1606, 2004. https://doi.org/10.1055/s-2004-813627.
23. Osman, N.F., Kerwin, W.S., McVeigh, E.R., and Prince, J.L., Cardiac motion tracking using CINE harmonic phase (HARP) magnetic resonance imaging. *Magn. Reson. Med.* 42:1048–1060, 1999. https://doi.org/10.1002/(SICI)1522-2594(199912)42:6<1048::AID-MRM9>3.0.CO;2-M.
24. Stoeck, C.T., Kalinowska, A., von Deuster, C., Harmer, J., Chan, R.W., Niemann, M., Manka, R., Atkinson, D., Sosnovik, D.E., Mekkaoui, C., and Kozerke, S., Dual-phase cardiac diffusion tensor imaging with strain correction. *PLoS One*. 9(9):e107159, 2014. https://doi.org/10.1371/journal.pone.0107159.
25. Sung, Y.M., and Yong, H., Myocardial T1 and T2 mappings with automatic motion correction at 3 tesla MR: Comparison of T1 and T2 measurements by breathhold, free-breathing and cardiac cycle. *J. Cardiovasc. Magn. Reson.* 15(1):P104, 2013. https://doi.org/10.1186/1532-429X-15-S1-P104.
26. Camargo, G.C., Rothstein, T., Junqueira, F.P., Fernandes, E., Greiser, A., Strecker, R., Pessoa, V., Lima, R.S., and Gottlieb, I., Comparison of myocardial T1 and T2 values in 3 T with T2* in 1.5 T in patients with iron overload and controls. *Int. J. Hematol.* 103:530, 2016. https://doi.org/10.1007/s12185-016-1950-1.
27. Osman, N.F., McVeigh, E.R., and Prince, J.L., Imaging heart motion using harmonic phase MRI. *IEEE Trans. Med. Imaging*. 19(3):186–202, 2000. https://doi.org/10.1109/42.845177.
28. Atalar, E., and McVeigh, E.R., Optimization of tag thickness for measuring position with magnetic resonance imaging. *IEEE Trans Med Imag*. 13(1):152–160, 1994. https://doi.org/10.1109/42.276154.
29. Young, A.A., and Axel, L., Three-dimensional motion and deformation of the heart wall: Estimation with spatial modulation of magnetization – a model-based approach. *Radiology*. 185(1):241–247, 1992. https://doi.org/10.1148/radiology.185.1.1523316.
30. Guttman, M.A., Prince, J.L., and McVeigh, E.R., Tag and contour detection in tagged MR images of the left ventricle. *IEEE Trans Med Imag*. 13(1):74–88, 1994. https://doi.org/10.1109/42.276146.
31. Denney, T.S., Identification of myocardial tags in tagged MR images without prior knowledge of myocardial contours. *Proc. Inform .Processing. Med. Imag.* 327–340, 1997. https://doi.org/10.1007/3-540-63046-5_25.
32. Acosta-Martínez, J., López-Haldón, J.E., Gutiérrez-Carretero, E., Díaz-Carrasco, I., Hajam, T.S., and Fernández, A.O., Radial and circumferential strain as markers of fibrosis in an experimental model of myocardial infarction. *Rev. Esp. Cardiol.* 66(6):508–509, 2013. https://doi.org/10.1016/j.rec.2013.01.009.

33. Nishimura, K., Okayama, H., Inoue, K., Saito, M., Yoshii, T., Hiasa, G., Sumimoto, T., Inaba, S., Ogimoto, A., Funada, J.I., and Higaki, J., Direct measurement of radial strain in the inner-half layer of the left ventricular wall in hypertensive patients. *J. Cardiol.* 59(1):64–71, 2012. https://doi.org/10.1016/j.jjcc.2011.08.003.
34. Ma, C., Wang, X., and Varghese, T., Segmental analysis of cardiac short-axis views using lagrangian radial and circumferential strain. *Ultrason. Imaging.* 38(6):363–383, 2016. https://doi.org/10.1177/0161734615613322.
35. Hoit, B.D., Strain and strain rate echocardiography and coronary artery disease. *Circ. Cardiovasc. Imaging.* 4(2):179–190, 2011. https://doi.org/10.1161/CIRCIMAGING.110.959817.